Computational Mechanics
https://doi.org/10.1007/s00466-023-02437-1

ORIGINAL PAPER

An enhanced corotational Virtual Element Method for large displacements in plane elasticity

Marco Nale[1] · Cristina Gatta[2] · Daniela Addessi[2] · Elena Benvenuti[1] · Elio Sacco[3]

Received: 20 July 2023 / Accepted: 12 December 2023

Abstract
An enhanced virtual element formulation for large displacement analyses is presented. Relying on the corotational approach, the nonlinear geometric effects are introduced by assuming nodal large displacements but small strains in the element. The element deformable behavior is analyzed with reference to the local system, corotating with the element during its motion. Then, the large displacement-induced nonlinearity is accounted for through the transformation matrices relating the local and global quantities. At the local level, the Virtual Element Method is adopted, proposing an enhanced procedure for strain interpolation within the element. The reliability of the proposed approach is explored through several benchmark tests by comparing the results with those evaluated by standard virtual elements, finite element formulations, and analytical solutions. The results prove that: (i) the corotational formulation can be efficiently used within the virtual element framework to account for geometric nonlinearity in the presence of large displacements and small strains; (ii) the adoption of enhanced polynomial approximation for the strain field in the virtual element avoids, in many cases, the need for ad-hoc stabilization procedures also in the nonlinear geometric framework.

Keywords Virtual element method · Corotational approach · Stabilization-free

1 Introduction

The structural analysis in the presence of large displacements can be carried out by different approaches, including more established Finite Element (FE) methods integrating the Total and Updated Lagrangian formulation, and the Corotational (CR) approach.

Pioneered by the seminal papers by Wempner [1], Belytschko and Hsieh [2], and Argyris and his collaborators [3], the key idea of the CR approach is to account for the effects of large displacements and rotations by decomposing the kinematics into a contribution provided by the large rigid-body displacements and the small-strain part. The CR approach has gained an ever-increasing interest in the computational mechanics community for it may reach results comparable to those obtainable through finite strain formulations. It offers indeed higher accuracy with respect to finite strain formulations and other approaches based on the small strain assumption and considering large displacements [4]. Another advantage is that the CR formulation obeys the principle of material frame indifference [5, 6] and can deal very simply with material nonlinear laws [7].

CR formulations were developed for one, two- and three-dimensional finite elements, such as beams [8, 9], plates [10, 11], shells [12], and bricks [13, 14], while unified CR formulations for general elements are also available [13, 15]. The CR approach has been exploited in various fields of structural analysis, including applications to masonry walls both

✉ Marco Nale
marco.nale@unife.it

Cristina Gatta
cristina.gatta@uniroma1.it

Daniela Addessi
daniela.addessi@uniroma1.it

Elena Benvenuti
elena.benvenuti@unife.it

Elio Sacco
elio.sacco@unina.it

[1] Department of Engineering, University of Ferrara, via Saragat 1, Ferrara 44122, Italy

[2] Department of Structural and Geotechnical Engineering, Sapienza University of Rome, via Eudossiana 18, 00184 Rome, Italy

[3] Department of Structures for Engineering and Architecture, University of Naples Federico II, via Claudio 21, 80125 Naples, Italy

Published online: 13 January 2024

using beams [16, 17] and bricks elements [14], shells made of shape-memory alloys [18], thin and moderately thick laminated composite structures [19], and soft biological tissues [20]. Variants are represented by the Implicit Corotational Method [21] to generate accurate geometrically nonlinear models, while Yaw and Sukumar [22] have extended the CR approach to the Maximum Entropy Meshfree Method [23].

However, the CR approach has been not yet extended to new generation generalized Galerkin finite element methods, such as the Mimetic Element Method [24], the Polygonal Finite Element Method [25–27], and the Virtual Element Method (VEM). Recently derived by Brezzi, Beirao, and coworkers [28] from the Mimetic Element Method, since its appearance, VEM has captured the general interest for it allows using general polygonal elements while completely releasing the meshing process from the requirement of generating regular undistorted meshes and avoiding hanging nodes. VEM was applied to a broad range of structural problems in linear [29], nonlinear [30], and finite elasticity and elastoplasticity [31], in elastodynamics, and fracture [32–34].

Classical VEM requires stabilization, which can be carried out through one of the various stabilization techniques proposed in the literature, examples being the stabilization technique proposed by Beirão da Veiga et al. [28], Chi et al. [35], and the locking-free technique devised by Wriggers et al. [36]. As the unique identification of the stabilization parameters may be a hard task, while being occasionally problem-dependent, stabilization-free VEM formulations have been recently developed [37] which combine low-order displacement interpolations and high-order strain descriptions. Indeed, it is known that a meaningful advance in terms of computational efficiency and high accuracy in bending-dominated situations and even in the nearly-incompressible limit can be reached by utilizing *enhanced* formulations for low-order finite element interpolations. The relevant seminal enhanced formulations can be retraced back to the assumed strain-based approach [38, 39], the B-bar methods [40–42], and the mode-decomposition and Hu–Washizu methods of Belytschko and co-workers [43]. Owing to their versatility, soon after their development, enhanced strain FE formulations were extended to geometrically non-linear problems [44], including a seminal CR-like approach [10].

Recently, it has been shown that the enhanced strain approach offers analogous advantages in the context of VEM [45], including the ability to deal with irregular meshes and improve accuracy, even for nearly incompressible materials. Of particular interest are the recent extensions of the enhanced strain approach to self-stabilized VE formulations. The key idea is to keep low the interpolation order even in the presence of many displacement degrees of freedom (DOFs) on the element boundary, as typical of polygonal VEs [45]. Another stabilization-free VE formulation, that does not require any additional internal DOFs and admits higher-order strain approximation, has been recently derived using Serendipity elements [46]. Similarly, a VEM based on the Hu–Washizu mixed variational principle has been recently proposed for 2D linear elastostatic framework [47]. The most notable advantage of this formulation is the possibility to prescribe the strain model a priori so that self-stabilized and locking-free low-order VEs with an accurate strain description can be obtained.

In the present contribution, for the first time, the CR formulation is implemented within an enhanced, stabilization-free, VEM framework for plane elasticity. In particular, the stabilization-free enhanced VEM developed by D'Altri et al. [45] is extended by exploiting a divergence-free polynomial approximation.

The paper is organized as follows. Section 2 details the strong and weak formulations of the problem. Section 3 is dedicated to presenting the CR approach. Section 4 describes the adopted enhanced virtual element formulation (EVE). Section 5 shows some numerical examples with a comprehensive discussion of the results. Finally, the salient conclusions and possible areas for further development are drawn in Sect. 6.

2 Problem formulation

The fundamental equations governing the two-dimensional (2D) continuum problem are described in the following.

A 2D domain $\Omega \subset \mathbb{R}^2$ is considered with its boundary $\partial\Omega$ constituted by $\Gamma_u \cup \Gamma_t = \partial\Omega$ and $\Gamma_u \cap \Gamma_t = \emptyset$, where Γ_u and Γ_t are the portions where displacements $\bar{\mathbf{u}}$ and tractions $\mathbf{t}$ are imposed, respectively. The problem is governed by the following strong form of compatibility and constitutive equations:

$$\begin{aligned} \boldsymbol{\varepsilon} &= \mathbf{D}\mathbf{u} \\ \boldsymbol{\sigma} &= \mathbf{C}\boldsymbol{\varepsilon} \end{aligned} \tag{1}$$

where $\boldsymbol{\varepsilon}$ and $\boldsymbol{\sigma}$ are the strain and stress organized in vectors according to the Voigt notation, $\mathbf{u}$ is the displacement vector, $\mathbf{D}$ is the compatibility operator, and $\mathbf{C}$ the material constitutive matrix. The elastic isotropic constitutive behavior is herein assumed. The above equations are complemented by the following Dirichlet and Neumann boundary conditions, that is:

$$\mathbf{u} = \bar{\mathbf{u}} \quad \text{on } \Gamma_u \tag{2}$$

$$\mathbf{N}\boldsymbol{\sigma} = \mathbf{t} \quad \text{on } \Gamma_t \tag{3}$$

where $\mathbf{N}$ contains the outward to Ω unit normal vector. To derive the approximated VEM procedure, the weak form of

the equilibrium equations is required, which is written by resorting to the virtual work principle as:

$$\text{Find } \mathbf{u} \in \mathcal{U} \text{ such that}$$
$$\int_\Omega (\mathbf{D}\delta\mathbf{u})^T\, \mathbf{C}\mathbf{D}\mathbf{u}\, d\Omega = \int_\Omega \delta\mathbf{u}^T\, \mathbf{b}\, d\Omega + \int_{\Gamma_t} \delta\mathbf{u}^T\, \mathbf{t}\, d\Gamma \quad \forall \delta\mathbf{u} \in \mathcal{U}_0 \tag{4}$$

with:

$$\mathcal{U} = \left\{ \mathbf{u} \in \left[H^1(\Omega) \right]^2 : \mathbf{u} = \overline{\mathbf{u}} \text{ on } \Gamma_u \right\} \tag{5}$$

$$\mathcal{U}_0 = \left\{ \delta\mathbf{u} \in \left[H^1(\Omega) \right]^2 : \delta\overline{\mathbf{u}} = \mathbf{0} \text{ on } \Gamma_u \right\} \tag{6}$$

and $\mathbf{b}$ and $\mathbf{t}$ denoting the body force and traction vectors.

For the considered 2D problem, $\mathbf{u} = \{u\, v\}^T$, $\mathbf{b} = \left\{b_x\, b_y\right\}^T$, $\overline{\mathbf{u}} = \{\overline{u}\, \overline{v}\}^T$, $\mathbf{t} = \left\{t_x\, t_y\right\}^T$, $\boldsymbol{\varepsilon} = \left\{\varepsilon_x\, \varepsilon_y\, \gamma_{xy}\right\}^T$, $\boldsymbol{\sigma} = \left\{\sigma_x\, \sigma_y\, \tau_{xy}\right\}^T$.

3 Corotational formulation for the enhanced virtual element

The 2D solid occupying the body Ω is discretized into nonoverlapping polygons. Each polygon E is characterized by the area Ω_E and boundary $\partial\Omega_E$, which is made up of n_V vertices, n_E edges and n nodes required for the displacement interpolation on the element boundary. Large displacement and small strain assumptions are considered to develop the enhanced VEM presented. The corotational formulation is introduced to this end by making reference to polygonal elements. In what follows, the procedure proposed by Battini et al. [11] for quadrilateral elements is extended to more general polygons. The overall motion of the polygonal virtual element E is expressed as the composition of the rigid (Fig. 1a) and deformation part (Fig. 1b). With reference to the global coordinate system $(O,\ X,\ Y)$ (Fig. 1), the current location of the node i is denoted by $\mathbf{X}_i = \{X_i\ Y_i\}^T$, and that referred to the initial undeformed configuration by $\mathbf{X}_i^0 = \left\{X_i^0\ Y_i^0\right\}^T$. Thus, the global displacement at node i is defined as:

$$\mathbf{U}_i = \mathbf{X}_i - \mathbf{X}_i^0 \tag{7}$$

and that of the element centroid C results:

$$\mathbf{U}_C = \mathbf{X}_C - \mathbf{X}_C^0 \tag{8}$$

The rigid motion can be expressed as the composition of the rigid translation, expressed by vector $\mathbf{U}_C$, and the rigid rotation θ (Fig. 1a). The varied position of the element, after rigid body motion, is considering as the 'corotational' reference configuration. Referring to this latter, that is the local corotated system $(C,\ x,\ y)$, the deformation displacement at node i is expressed as:

$$\tilde{\mathbf{V}}_i = \mathbf{x}_i - \mathbf{x}_i^0 \tag{9}$$

where $\mathbf{x}_i$ indicates the local position of node i as referred to the corotated reference system after the deformation process and $\mathbf{x}_i^0$ its initial position in the same system. In Eq. 9 the current local position $\mathbf{x}_i$ can be evaluated as:

$$\mathbf{x}_i = \mathbf{R}(\mathbf{X}_i - \mathbf{X}_C) \tag{10}$$

where $\mathbf{R}$ is the matrix ruling the rigid rotation tranformation from the initial global reference system to the local one, expressed as:

$$\mathbf{R} = \begin{bmatrix} \cos\theta & \sin\theta \\ -\sin\theta & \cos\theta \end{bmatrix} \tag{11}$$

By introducing Eq. 10 in 9, and using Eqs. 7 and 8, it follows:

$$\tilde{\mathbf{V}}_i = \mathbf{R}\left(\mathbf{U}_i + \mathbf{X}_i^0 - \mathbf{U}_C - \mathbf{X}_C^0\right) - \mathbf{x}_i^0 \tag{12}$$

The rigid rotation θ is evaluated by minimizing the square of the Euclidean norm of the nodal deformation displacements and results:

$$\tan\theta = \frac{\sum_{i=1}^n x_i^0 (Y_i - Y_C) - y_i^0 (X_i - X_C)}{\sum_{i=1}^n \mathbf{x}_i^{0\,T} (\mathbf{X}_i - \mathbf{X}_C)} \tag{13}$$

The global and local deformation displacement vectors at all the nodes of each element are collected in vectors $\mathbf{U}$ and $\tilde{\mathbf{V}}$, respectively. The following relation links their variations:

$$\delta\tilde{\mathbf{V}} = \mathbf{B}\,\delta\mathbf{U} \tag{14}$$

where $\mathbf{B}$ is the compatibility operator defined in the following. Considering the local deformation displacement at node i, it results:

$$\delta\tilde{\mathbf{V}}_i = \mathbf{R}\,(\delta\mathbf{X}_i - \delta\mathbf{X}_C) + \delta\mathbf{R}\,(\mathbf{X}_i - \mathbf{X}_C) - \delta\mathbf{x}_i^0 \tag{15}$$

and, after some manipulations, it is obtained:

$$\delta\tilde{\mathbf{V}}_i = \mathbf{R}\,(\delta\mathbf{U}_i - \delta\mathbf{U}_C) - \mathbf{Y}_i\,\delta\theta \tag{16}$$

with:

$$\mathbf{Y}_i = \begin{Bmatrix} -y_i \\ x_i \end{Bmatrix} \tag{17}$$

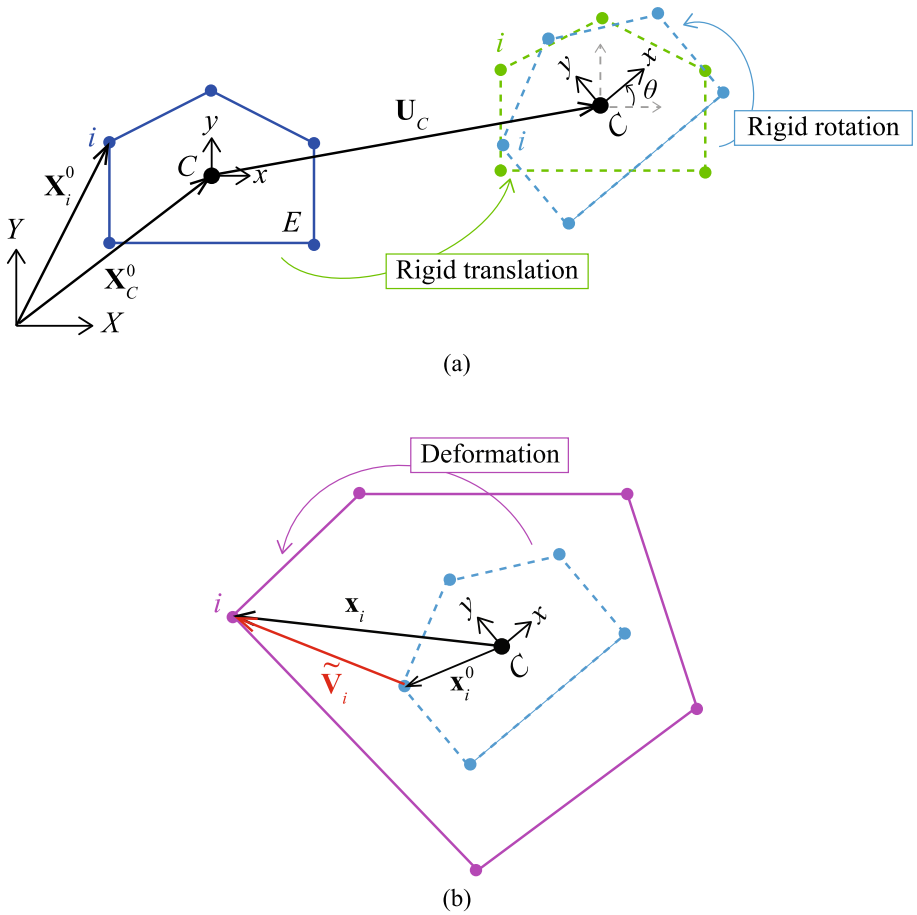

Fig. 1 Kinematics of the virtual element: (a) rigid and (b) deformation parts

The variation of the rigid rotation $\delta\theta$ is evaluated as:

$$\delta\theta = \sum_{i=1}^{n} \frac{1}{\sum_{i=1}^{n} \mathbf{x}_i^{0\,T}\mathbf{x}_i} \mathbf{Y}_i^{0T}\,\mathbf{R}\,(\delta\mathbf{U}_i - \delta\mathbf{U}_C) \tag{18}$$

where:

$$\mathbf{Y}_i^0 = \begin{Bmatrix} -y_i^0 \\ x_i^0 \end{Bmatrix} \tag{19}$$

Introducing Eq. 18 in Eq. 16, it results:

$$\delta\tilde{\mathbf{V}} = (\mathbf{I} - \mathbf{AG})\mathbf{E}^T\,\delta\mathbf{U} \tag{20}$$

where matrix $\mathbf{E}$ is the $2n \times 2n$ operator collecting the rotation matrices, i.e.:

$$\mathbf{E} = \begin{bmatrix} \mathbf{R}^T & \mathbf{0} & \dots & \mathbf{0} \\ \mathbf{0} & \mathbf{R}^T & & \vdots \\ \vdots & & \ddots & \vdots \\ \mathbf{0} & \dots & \dots & \mathbf{R}^T \end{bmatrix} \tag{21}$$

Matrix $\mathbf{A} = \left\{\mathbf{Y}_1^T\,\mathbf{Y}_2^T \dots \mathbf{Y}_n^T\right\}^T$ collects vectors $\mathbf{Y}_i$ for all the nodes located on the element boundary, and:

$$\mathbf{G} = \frac{1}{\sum_{i=1}^{n} \mathbf{x}_i^{0\,T}\mathbf{x}_i}\mathbf{A}^0 \tag{22}$$

with $\mathbf{A}^0 = \left\{\mathbf{Y}_1^{0T}\,\mathbf{Y}_2^{0T} \dots \mathbf{Y}_n^{0T}\right\}$. The transformation matrix $\mathbf{B}$ in Eq. 14 is then defined as follows:

$$\mathbf{B} = (\mathbf{I} - \mathbf{AG})\,\mathbf{E}^T \tag{23}$$

with $\mathbf{I}$ denoting the identity matrix. The nodal forces work-conjugate to displacement global and local vectors, $\mathbf{U}$ and $\tilde{\mathbf{V}}$, are collected in vectors $\mathbf{P}$ and $\tilde{\mathbf{P}}$ and are linked by the following relation:

$$\delta\mathbf{P} = \mathbf{B}^T\,\delta\tilde{\mathbf{P}} \tag{24}$$

derived by invoking the equivalence of the element virtual work evaluated at the global and local level, respectively. The incremental relation between the global force and displacement vectors is:

$$\delta\mathbf{P} = \frac{\partial\mathbf{P}}{\partial\mathbf{U}}\delta\mathbf{U} \tag{25}$$

Considering the incremental force-displacement relation at the element local level in the form:

$$\delta\tilde{\mathbf{P}} = \tilde{\mathbf{K}}\,\delta\tilde{\mathbf{V}} \tag{26}$$

and making use of Eqs. 14 and 24, it follows:

$$\frac{\partial \mathbf{P}}{\partial \mathbf{U}} = \frac{\partial(\mathbf{B}^T\,\tilde{\mathbf{P}})}{\partial \mathbf{U}} = \mathbf{B}^T\,\frac{\partial \tilde{\mathbf{P}}}{\partial \tilde{\mathbf{V}}}\,\frac{\partial \tilde{\mathbf{V}}}{\partial \mathbf{U}} + \frac{\partial \mathbf{B}^T}{\partial \mathbf{U}}\,\tilde{\mathbf{P}} = \mathbf{B}^T\,\tilde{\mathbf{K}}\,\mathbf{B} + \mathbf{K}_g \tag{27}$$

where the first term at the RHS indicates the material tangent matrix, while the second term is the geometric tangent matrix defined as:

$$\mathbf{K}_g = \delta\mathbf{E}\,(\mathbf{I} - \mathbf{AG})^T\,\tilde{\mathbf{P}} + \mathbf{E}\,\delta(\mathbf{I} - \mathbf{AG})^T\,\tilde{\mathbf{P}} \tag{28}$$

4 Enhanced virtual element method

The enhanced VEM formulation presented in [45] is here adopted and the main steps are recalled in the following. The virtual displacement field $\mathbf{v}$ at the generic point in the element domain Ω_E, according to the corotational approach, is the approximated deformation displacement as referred to the local corotated system $(C,\ x,\ y)$, defined as (see Eq. 12):

$$\mathbf{v} = \mathbf{R}\left(\mathbf{U} + \mathbf{X}^0 - \mathbf{U}_C - \mathbf{X}_C^0\right) - \mathbf{x}^0 \tag{29}$$

According to the classical VEM assumptions, the displacement field $\mathbf{v}$ is not explicitly interpolated. Conversely, the approximated displacement field $\tilde{\mathbf{v}}$ on the element boundary $\partial\Omega_E$ is expressed as function of the displacement degrees of freedom defined at the n nodes lying on it by means of prescribed shape functions collected in matrix $\mathbf{N}^V$. The assumed interpolation of $\tilde{\mathbf{v}}$ is written as:

$$\tilde{\mathbf{v}} = \mathbf{N}^V\,\tilde{\mathbf{V}} \tag{30}$$

where vector $\tilde{\mathbf{V}}$ has $2n_V k$ components, with k denoting the order of the polynomial interpolation adopted. To obtain a suitable representation of the approximated strain associated to the unknown virtual displacement, $\mathbf{v}$, in the element interior, the projected strain $\boldsymbol{\varepsilon}^P$ is defined as the unique function that minimizes the energy norm, that is the solution of the following equation:

$$\int_{\Omega_E} (\delta\boldsymbol{\varepsilon}^P)^T\,\mathbf{C}\,\left(\boldsymbol{\varepsilon}^P - \mathbf{Dv}\right)\,d\Omega_E = 0 \quad \forall\,\delta\boldsymbol{\varepsilon}^P \in \mathcal{P}^q(\Omega_E) \tag{31}$$

where $\mathcal{P}^q(\Omega_E)$ indicates the polynomial space up to order q. Denoting with $\boldsymbol{\sigma}^P$ the stress vector associated to the strain $\boldsymbol{\varepsilon}^P$, Eq. 31 can be expressed as follows:

$$\int_{\Omega_E} (\mathbf{C}^{-1}\delta\boldsymbol{\sigma}^P)^T\left(\boldsymbol{\sigma}^P - \mathbf{CDv}\right)\,d\Omega_E = 0 \quad \forall\,\delta\boldsymbol{\sigma}^P \in \mathcal{P}^q(\Omega_E) \tag{32}$$

Then, the stress vector $\boldsymbol{\sigma}^P$ is interpolated on the basis of the parameters contained in vector $\hat{\boldsymbol{\sigma}}$ and the polynomial functions collected in the matrix $\check{\mathbf{N}}$, that is:

$$\boldsymbol{\sigma}^P = \check{\mathbf{N}}\,\hat{\boldsymbol{\sigma}} \tag{33}$$

By introducing the interpolation expressed by Eq. 33 in Eq. 32 and integrating by parts this latter term, the following expression results for the stress parameters:

$$\hat{\boldsymbol{\sigma}} = \left[\int_{\Omega_E} \check{\mathbf{N}}^T\mathbf{C}^{-1}\check{\mathbf{N}}\,d\Omega_E\right]^{-1} \left[\int_{\partial\Omega_E} (\mathbf{N}_E^T\check{\mathbf{N}})^T\,\mathbf{N}^V\,d\Gamma_E\,\tilde{\mathbf{V}} - \int_{\Omega_E} (\mathbf{D}^T\check{\mathbf{N}})^T\,\mathbf{v}\,d\Omega_E\right] \tag{34}$$

where $\mathbf{N}_E$ is the matrix containing the direction cosines of the outward unit normal vectors on Γ_E.
Assuming the following definitions:

$$\begin{aligned} \mathcal{G} &= \int_{\Omega_E} \check{\mathbf{N}}^T\mathbf{C}^{-1}\check{\mathbf{N}}\,d\Omega_E \\ \tilde{\mathcal{B}}\,\tilde{\mathbf{V}} &= \int_{\partial\Omega_E} (\mathbf{N}_E^T\check{\mathbf{N}})^T\,\mathbf{N}^V\,d\Gamma_E\,\tilde{\mathbf{V}} \\ \hat{\mathcal{B}}\,\hat{\mathbf{V}} &= -\int_{\Omega_E} (\mathbf{D}^T\check{\mathbf{N}})^T\,\mathbf{v}\,d\Omega_E \end{aligned} \tag{35}$$

Equation 34 can be written in compact form as follows:

$$\hat{\boldsymbol{\sigma}} = \mathcal{G}^{-1}\left(\tilde{\mathcal{B}}\tilde{\mathbf{V}} + \hat{\mathcal{B}}\hat{\mathbf{V}}\right) \tag{36}$$

with vector $\hat{\mathbf{V}}$ collecting the moments of the virtual displacement $\mathbf{v}$ representing additional internal degrees of freedom.

After the evaluation of the stress parameters by Eq. 36, the projected strain $\boldsymbol{\varepsilon}^P$ is computed as:

$$\boldsymbol{\varepsilon}^P = \mathbf{C}^{-1}\check{\mathbf{N}}\hat{\boldsymbol{\sigma}} \tag{37}$$

The LHS term in the virtual work equation in Eq. 4, expressing the internal work, can now be written in each element domain as a function of the projected strain $\boldsymbol{\varepsilon}^P$, resulting as:

$$\int_{\Omega_E} [\boldsymbol{\varepsilon}^P(\delta\mathbf{v})]^T\,\mathbf{C}\boldsymbol{\varepsilon}^P(\mathbf{v})\,d\Omega_E = \int_{\Omega_E} \left(\mathcal{G}^{-1}\mathcal{B}\,\delta\mathbf{V}\right)^T\,\check{\mathbf{N}}^T\mathbf{C}^{-1}\check{\mathbf{N}}\mathcal{G}^{-1}\mathcal{B}\,\mathbf{V}\,d\Omega_E \tag{38}$$

having collected:

$$\mathcal{B} = \begin{bmatrix} \tilde{\mathcal{B}} & \hat{\mathcal{B}} \end{bmatrix}, \ \mathbf{V} = \begin{bmatrix} \tilde{\mathbf{V}} & \hat{\mathbf{V}} \end{bmatrix}^T \tag{39}$$

Equation 38 can be manipulated as:

$$\delta \mathbf{V}^T \left[\mathcal{B}^T \mathcal{G}^{-T} \left(\int_{\Omega_E} \check{\mathbf{N}}^T \mathbf{C}^{-1} \check{\mathbf{N}} d\Omega_E \right) \mathcal{G}^{-1} \mathcal{B} \right] \mathbf{V} = \delta \mathbf{V}^T \tilde{\mathbf{K}}_c \mathbf{V} \tag{40}$$

where the consistent definition of the element stiffness matrix $\tilde{\mathbf{K}}_c$ is introduced. Among the different possible procedures to select the polynomial representation for $\check{\mathbf{N}}$, the divergence-free formulation is here adopted, corresponding to a self-equilibrated representation of $\boldsymbol{\sigma}^P$. This is a special choice that leads to no internal degrees of freedom, as the last term at the RHS of Eq. 34 vanishes being $\mathbf{D}^T \check{\mathbf{N}} = \mathbf{0}$. Results reported in [45] proved that this assumption allows to obtain satisfactory solutions, especially if no distributed volume forces are considered. The slightly worse results obtained in the presence of volume forces could be improved by selecting other types of polynomial representation for $\check{\mathbf{N}}$, which lead to more complex formulations involving also the internal degrees of freedom.

In the presented enhanced formulation, differently from the standard VEM, the degree q of the polynomial representation in $\check{\mathbf{N}}$ is not linked to the order k used in $\mathbf{N}^V$, but it is selected so that the number of modes considered in $\check{\mathbf{N}}$ is greater than or equal to the element degrees of freedom purged by the number of rigid motions (i.e., modes in $\check{\mathbf{N}} \geq n_{DOF} - 3$ in the presented 2D formulation). Appendix A shows the matrix $\check{\mathbf{N}}$ adopted in cases of $q = 1$, $q = 2$ and $q = 3$. In such a way, self-stabilized elements are derived for which the stabilization term is not required and, consequently, the stiffness matrix $\tilde{\mathbf{K}}$ is equal to $\tilde{\mathbf{K}}_c$ in Eq. 40.

To clarify, Table 1 reports the number of modes in $\check{\mathbf{N}}$ and the polynomial degree q to be taken for the single enhanced virtual element with n_V vertices and n_{DOF} degrees of freedom, assuming $k = 1$. For instance, if the element is characterized by $n_V = 4$ and $n_{DOF} = 8$, at least 5 parameters are needed to describe the strain field. Thus, the three strain components can be assumed linear ($q = 1$) into the element leading to 9 strain (or stress) parameters, that reduce to 7 by enforcing the free-divergence.

Table 1 Polynomial degree q to be adopted for the single element with n_V vertices and n_{DOF} degrees of freedom, and effective mode number of $\check{\mathbf{N}}$ for the divergence-free polynomial representation. (Table adapted from [45])

n_V	n_{DOF}	q	$\check{\mathbf{N}}$ modes
3	6	0	3
4	8	1	7
5	10	1	7
6	12	2	12
7	14	2	12
8	16	3	18
9	18	3	18
10	20	3	18

5 Numerical examples

This section aims to validate both the efficiency of the numerical procedure and the accuracy of the results obtained by employing the CR-EVE approach for a set of numerical examples in plane elasticity. These are properly selected from the literature for the sake of comparison with established formulations.

Four classical examples of structures exhibiting geometric nonlinear response are considered, namely, thin and thick cantilevers, an L-bracket beam, and a circular shallow arch.

For the EVE, the first-order ($k = 1$) displacement approximation is adopted, while the degree q of the strain interpolation varies according to the number of nodes of the element. For comparison purposes, the VEM stabilized according to the procedure proposed by Artioli et al. [29] is also considered.

Table 2 summarizes the relevant information useful for identifying, for each example, the operational data concerning the CR-EVE and the adopted reference solutions. The degrees of freedom (DOFs), the average diameter h_{av} of the element in the mesh are reported. Furthermore, in the case of the CR-EVE formulation, the polynomial degree q of the strain approximation is detailed. Acronyms identifying the various formulations are used for brevity. In particular, CR-VE-Q4 denotes a stabilized four-noded VE while incorporating the CR approach. On the other hand, CR-EVE-Q4 indicates the homologous enhanced VE. Similarly, the formulations based on Voronoi meshes, generated using Lloyd's iteration-based algorithm implemented in PolyMesher [48], are designated with the acronyms CR-VE-V and CR-EVE-V for the stabilized and enhanced self-stabilized VE formulation, respectively. From Table 2 it clearly emerges that VEs denoted with CR-VE-Q4 and CR-VE-V are based on the use of polynomial approximation of the strain field with order $q = 0$, while the CR-EVE-Q4 and CR-EVE-V elements are associated to $q = 1$ and $q = 2$, respectively.

As for the VE simulations, the solution of the nonlinear problem is determined by means of an incremental-iterative Newton Raphson method using the Modified Generalized Displacement Control (MGDC) method [50] with a convergence tolerance of 10^{-6}. The load–displacement curves obtained with the proposed approach are compared with both reference solutions provided by previously proposed CR-FE formulations [11, 22, 49, 51] and FE results obtained by Abaqus using overkill meshes made of 4-node CPS4

Table 2 Data concerning the adopted VE and FE formulations in terms of: used acronyms, DOFs, average diameter of the element, stabilization instances, and polynomial degree q of the strain approximation

Example	ID Element	DOFs	h_{av}	Stabilization	q
Thin cantilever	CR-VE-Q4	1280	0.0870	Yes	0
	CR-EVE-Q4	1280	0.0870	No	1
	CR-VE-V	1282	0.0920	Yes	0
	CR-EVE-V	1282	0.0920	No	2
	Hybrid Stress FEM [49]	126	n.a	n.a	n.a
	Abaqus-CSP4	21794	0.0182	n.a	n.a
Thick cantilever	CR-VE-Q4	1298	0.2641	Yes	0
	CR-EVE-Q4	1298	0.2641	No	1
	CR-VE-V	1280	0.3842	Yes	0
	CR-EVE-V	1280	0.3842	No	2
	Meshfree [22]	738	n.a	n.a	n.a
	Abaqus-CPS4	41730	0.0442	n.a	n.a
L-Bracket	CR-VE-Q4	772	0.3536	Yes	0
	CR-EVE-Q4	772	0.3536	No	1
	CR-VE-V	1218	0.3288	Yes	0
	CR-EVE-V	1218	0.3288	No	2
	Enhanced FEM [11]	772	n.a	n.a	n.a
	Abaqus-CPS4	10370	0.0884	n.a	n.a
Circular shallow arch	CR-VE-Q4	1390	27.0931	Yes	0
	CR-EVE-Q4	1390	27.0931	No	1
	CR-VE-V	2204	25.1400	Yes	0
	CR-EVE-V	2204	25.1400	No	2
	Meshfree [22]	5522	n.a	n.a	n.a
	Abaqus-CPS4	67650	3.5083	n.a	n.a

elements [52], based on bi-linear shape functions for the displacement interpolation and plane stress assumption in finite elasticity.

5.1 Cantilever beams

The first set of analyses investigates the structural response of cantilevers with two different slenderness ratios, corresponding to a thin and a thick cantilever subjected to uniform vertical load at the free end, illustrated in Sects. 5.1.1 and 5.1.2, respectively.

5.1.1 Thin cantilever

The response of a thin cantilever subjected to a shear load at the free end is analyzed assuming length $l = 10$ mm, height $h = 0.1478$ mm, and thickness $t = 0.1$ mm. Elastic material with Young's modulus $E = 10^8$ MPa and null Poisson's ratio is employed. The same problem was studied by Karkon and Rezaiee-Pajand [49] through a hybrid-stress FE formulation. Figure 2 shows the undeformed beam configuration and the boundary and loading conditions.

The adopted CR-EVE meshes consist of the same DOFs for quadrilateral and Voronoi elements, respectively. An

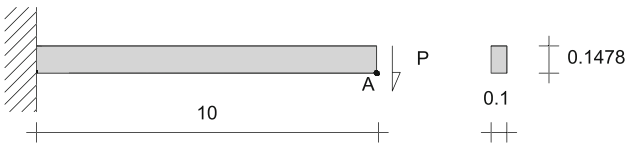

Fig. 2 Thin cantilever: geometry (dimensions are in millimeters), boundary and loading conditions

initial load factor $\overline{\Delta\lambda} = 10.0$ is set. Figure 3a shows the deformed geometry of the cantilever at the last load increment. The load–displacement curves, relating the vertical displacement of point A in Fig. 2 to the total applied force, for the different formulations adopted are displayed in Fig. 3b. The superior accuracy of the CR-EVE with respect to the classic stabilized VEM clearly emerges. It can be observed that the load–displacement curve obtained with the higher-order enhanced CR Voronoi elements (CR-EVE-V) overlaps with the reference solution obtained using the Abaqus overkill mesh (CPS4) and the hybrid-stress formulation proposed by Karkon et al. [49]. Conversely, the load–displacement curve obtained with the CR-EVE-Q4 is less accurate with the same number of DOFs. Finally, to demonstrate the robustness of CR-EVE formulation, Table 3

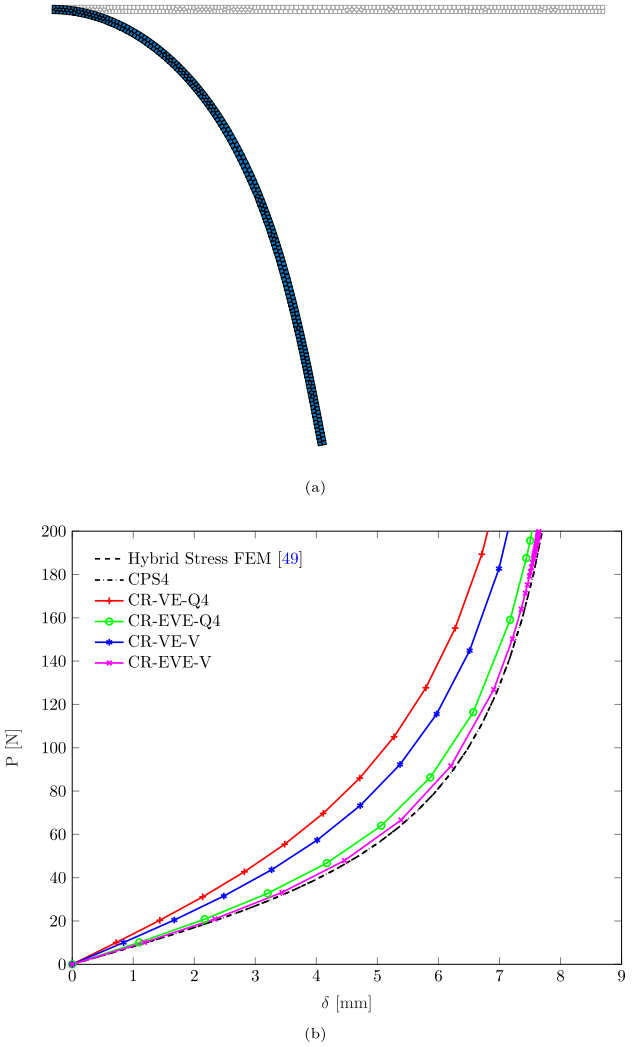

Fig. 3 Thin cantilever: **a** deformed configuration at the final step of the analysis and **b** load–displacement curves obtained with the standard and the CR-EVE compared with those derived from the hybrid stress FE formulation [49] and the Abaqus overkill mesh made of CPS4 FEs

shows the vertical displacement δ of the beam end section for variable DOFs with both quadrilateral and Voronoi meshes. The reference overkill-mesh result is also reported for the reader's convenience.

5.1.2 Thick cantilever

A thick cantilever, borrowed from Yaw et al. [22], is subjected to a shear load applied at the free end. The cantilever has a length $l = 10$ in, height $h = 2$ in, and thickness $t = 2$ in and is made of a material with Young's modulus $E = 100$ ksi and null Poisson ratio. Figure 4 shows the cantilever geometry, boundary and loading conditions.

The analysis is carried out with meshes of quadrilateral and polygonal virtual elements sharing the same DOFs. It has been verified that the use of 20000 quadrilateral CR-EVE-Q4 leads to an almost identical load–displacement profile. The computation of load–displacement curves, evaluated by monitoring the displacement of point A in Fig. 4, is performed with the MDGC with prescribed initial load factor $\overline{\Delta\lambda} = 0.2$. Figure 5a illustrates the deformed configuration of the thick cantilever, while Fig. 5b displays the load–displacement curves for different VE meshes and enhancement types.

Table 3 Thin cantilever: vertical displacement δ at $P = 200$ N for variable DOFs

ID Element	DOFs	h_{av}	δ [mm]
CR-VE-Q4	810	0.1303	5.794
CR-EVE-Q4	810	0.1303	7.243
CR-VE-V	812	0.1163	6.661
CR-EVE-V	812	0.1163	7.529
CR-VE-Q4	1280	0.0870	6.807
CR-EVE-Q4	1280	0.0870	7.534
CR-VE-V	1282	0.0920	7.137
CR-EVE-V	1282	0.0920	7.646
Abaqus-CPS4	21794	0.0182	7.699

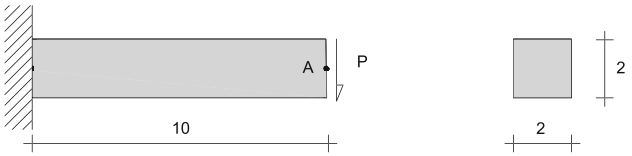

Fig. 4 Thick cantilever: geometry (dimensions are in inches), boundary and loading conditions

The current results match well both the analytical solution obtained by Yaw [51] for an Eulero-Bernoulli-beam assuming large displacements and axial deformations and that computed through a meshfree CR-formulation [22]. For completeness, the Abaqus solution obtained with an overkill mesh of CPS4 elements incorporating a finite elasticity formulation is also reported. It can be observed that, at least in the present example, the incidence of non-infinitesimal strains emerges at the final stages of the loading history, as soon as the deformed cantilever tends to take an almost vertical configuration so that any further change of configuration should be ascribed to axial finite elastic deformations rather than to large displacements and rotations, a circumstance where Total or Updated Lagrangian finite elasticity formulations are more accurate [15]. The example confirms nevertheless that the presented CR-EVE approach leads to satisfactory results in terms of accuracy with respect to the homologous reference numerical solutions even when coarse meshes are employed.

The influence of non-convex and distorted meshes on the robustness of the proposed CR-EVE formulation has been also tested. For this purpose, the meshes shown in Fig. 6, made of distorted quadrilateral elements (CR-EVE-Q4D),

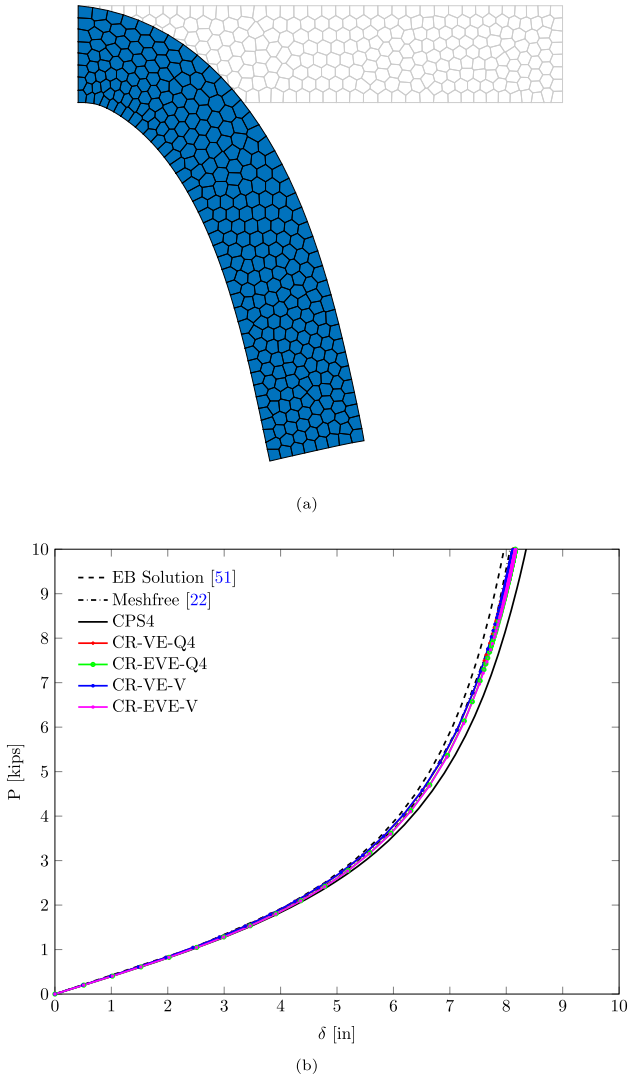

Fig. 5 Thick cantilever beam: **a** deformed configuration at the end of the analysis, **b** load–displacement curves obtained with the standard and the enhanced CR-VEM compared with the available analytical Euler–Bernoulli beam solution [51] and results derived from the meshfree CR-formulation [22] and the Abaqus overkill mesh made of CPS4 FEs

Voronoi Lloyd-iteration-based elements (CR-EVE-V), and non-convex elements (CR-EVE-NC) have been used. In Fig. 6, the regular quadrilateral mesh (CR-EVE-Q4) is also displayed for the sake of comparison. Further details, in terms of number of DOFs, polynomial degree q and average diameter h_{av} of the elements of the meshes, are reported in Table 4. The resulting load–displacement curves in Fig. 7 confirm that the proposed formulation performs well even with non-convex and distorted elements, as the results are not affected by the mesh type.

Analogously to the thin beam example, the beam free end vertical displacement is shown in Table 5 for all enhanced and classical formulations with both quadrilateral and Voronoi meshes with different DOFs number. The reference overkill-mesh result is also shown.

5.2 L-bracket

The third example is drawn from the paper of Battini [11] and involves the modeling of the bending behavior of the L-bracket shown in Fig. 8. The L-bracket is fixed at the top and it is subjected to a uniform shear load at the free end. Each branch has a length of 10 mm and a square cross-section. The elastic properties of the material are Young's modulus $E = 3 \times 10^7$ MPa, and Poisson ratio $\nu = 0.3$.

Meshes of 304 square and Voronoi elements are used for the analysis. Figure 9a reports the deformed shape at the last load increment, while the load–displacement curves for the various types of elements are reported in Fig. 9a. These are derived by relating the vertical displacement of point A at the free end (Fig. 8) to the applied load. The obtained solutions are computed with a prescribed initial load factor $\overline{\Delta\lambda} = 0.15$. The results are consistent with the Abaqus overkill mesh and the numerical solution obtained by Battini [11].

Notably, in general, the self-stabilized CR-EVE formulation exhibits greater accuracy than the standard stabilized one, providing global load–displacement curves overlapped to those derived from the other reference numerical approaches.

5.3 Shallow arch

The last studied structural example is illustrated in Fig. 10 and concerns the thin circular shallow arch previously studied by Yaw et al. [22] by means of a CR-meshless formulation. The arch is simply supported with hinges located at both ends along the axis line. A concentrated force is applied on the symmetry axis at the upper surface. The arch geometry is featured by radius $r = 10581.6$ mm, thickness $t = 79.2$ mm, depth $w = 25.4$ mm, and rise $f = 76.48$ mm, being the horizontal span length $l = 2540$ mm. The material is modeled assuming Young's modulus $E = 68.948\,\text{kN/mm}^2$ and null Poisson ratio.

Meshes made of quadrilateral and Voronoi elements are assumed, adopting the initial load factor $\overline{\Delta\lambda}$ equal to 1.5. Figure 11b shows the load–displacement curve of the considered shallow arch, which relates the force to the vertical displacement of its application point A.

The snap-through behavior is satisfactorily captured, as shown by the comparison with the reference solutions derived from Abaqus with an overkill mesh of CPS4 elements and the CR meshless approach developed by Yaw et al. [22]. In particular, the results confirm that accuracy greatly improves when the enhanced VEM is employed instead of the classical VEM with stabilization. It is suggested that the slight discrepancies between the comparison and the present curves

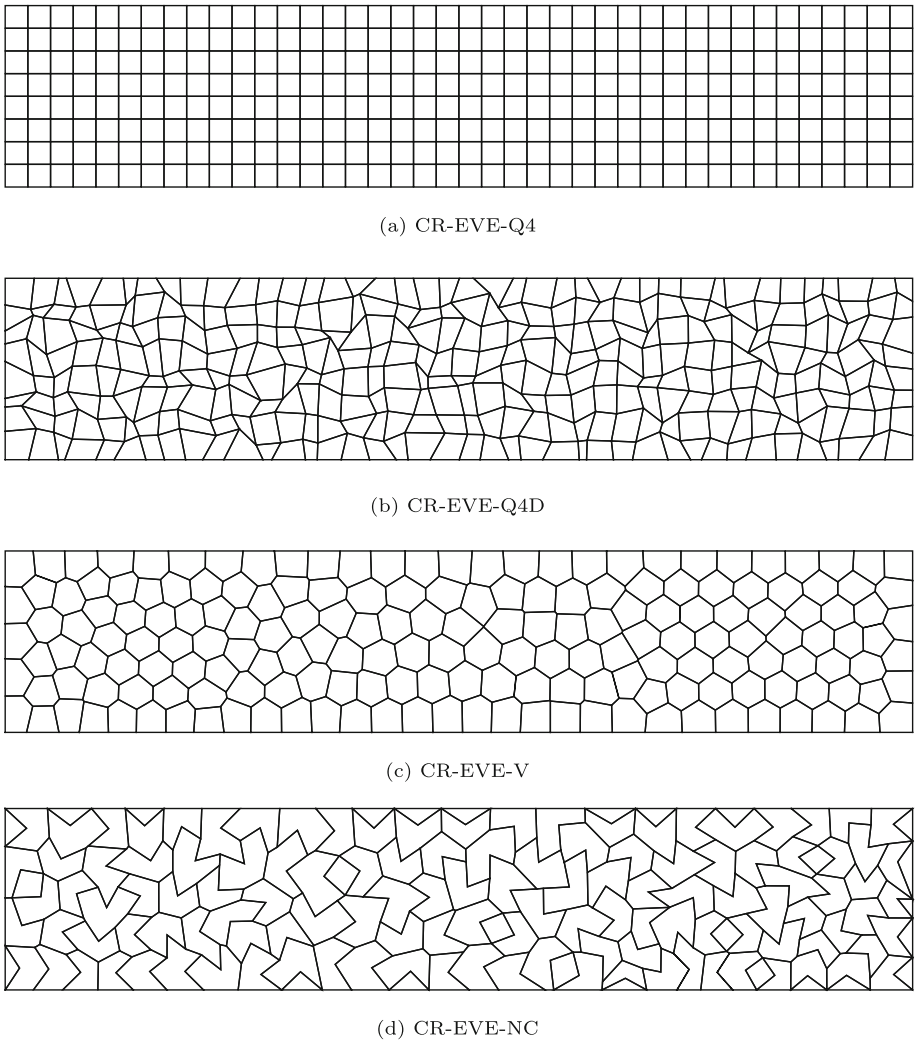

(a) CR-EVE-Q4

(b) CR-EVE-Q4D

(c) CR-EVE-V

(d) CR-EVE-NC

Fig. 6 Meshes adopted for the thick cantilever: **a** quadrilateral elements, **b** distorted quadrilateral elements, **c** Voronoi Lloyd-iteration-based elements, **d** non-convex elements

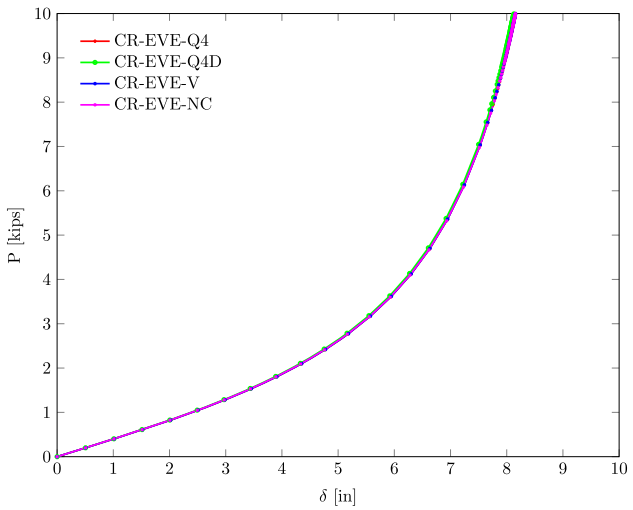

Fig. 7 Thick cantilever: load–displacement curves derived from the meshes shown in Fig. 6 and featured by Table 4

Table 4 Thick cantilever: features of the meshes shown in Fig. 6

ID Element	DOFs	h_{av}	q
CR-EVE-Q4	738	0.3536	1
CR-EVE-Q4D	738	0.4055	1
CR-EVE-V	736	0.4372	2
CR-EVE-NC	736	0.5919	3

observable at the lower and upper limit points could be ascribed to the usage of force-based versus displacement-based arc length algorithms, as already observed by Pretti et al. [53]. It should be, indeed, recalled that, due to the presence of snap-back and snap-through critical points, the issue of tracing the nonlinear structural response of loaded arches is one of the most challenging in computational mechanics. A thorough discussion of the performance of the available arc-length algorithms, such as the one provided in [53], is out of the aims of the present paper, the present focus being on the investigation of the effective gain in terms of accuracy

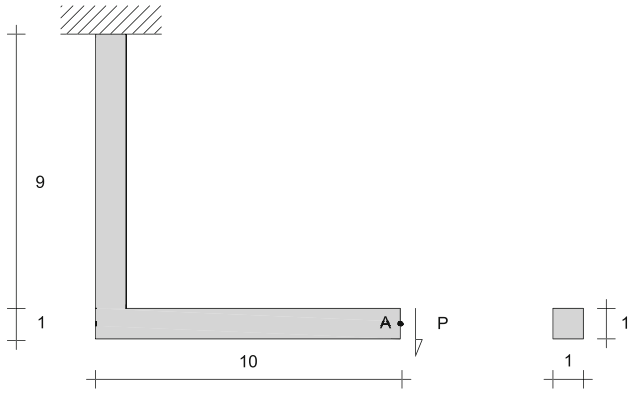

Fig. 8 L-bracket: geometry (dimensions are in millimeters), boundary and loading conditions

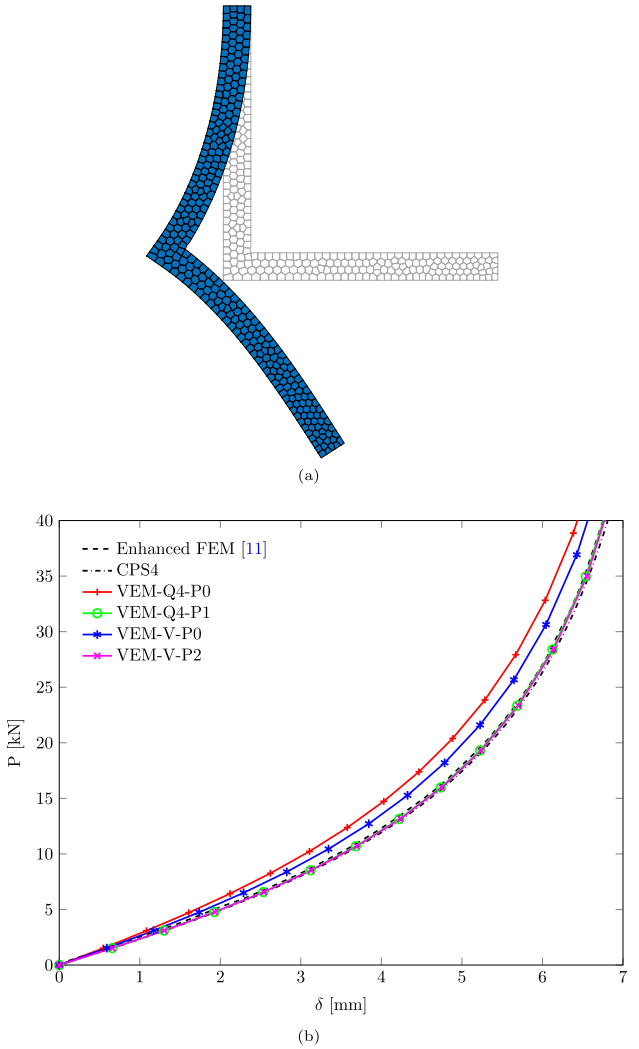

Fig. 9 L-bracket: **a** deformed configuration at the end of the analysis, and **b** load–displacement curves obtained with standard and enhanced CR-VEM compared with the reference solutions obtained utilizing the enhanced CR-FE formulation proposed by Battini [11] and the Abaqus overkill mesh made of CPS4 FEs

Table 5 Thick cantilever: vertical displacement δ at $P = 10$ kips for variable DOFs

ID Element	DOFs	h_{av}	δ [in]
CR-VE-Q4	738	0.3536	8.089
CR-EVE-Q4	738	0.3536	8.154
CR-VE-V	736	0.4372	8.085
CR-EVE-V	736	0.4372	8.156
CR-VE-Q4	1298	0.2611	8.125
CR-EVE-Q4	1298	0.2611	8.161
CR-VE-V	1280	0.3842	8.122
CR-EVE-V	1280	0.3842	8.166
Abaqus-CPS4	41730	0.0442	8.3518

brought by the adoption of the enhancement technology proposed in the present corotational VE formulation with respect to the classical stabilized VEM.

Remarkably, from the present results, it can be inferred that a comparatively reduced number of elements allows us to accurately capture the reference solution. For completeness, Figs. 12a, b highlight the critical points of the load–displacement results obtained using CR-EVE-Q4 elements with 1390 DOFs, including the snap-through points A and B, the inferior limit point C, the inflection point D, and the corresponding deflection evolution for variable non-dimensional span length x/l, respectively.

6 Conclusion

A corotational framework for plane virtual elements was presented. According to the key idea of the corotational approach, the kinematics of the virtual element was decomposed in its rigid and deformation parts by introducing a local/corotated system moving with the element during its motion. Hence, the deformable element response, described in terms of element stresses and stiffness, was evaluated on the basis of the small deformation displacements referred to the corotational system, whereas the large displacement-induced nonlinearity was considered through the transformation matrices relating to the local and global quantities. This permitted to account for nonlinear geometric effects, still assuming small strains at the element level. Moreover, linear elastic material behavior was considered. As for the virtual element formulation, low-order displacement interpolation was assumed, while considering an enhanced strain description. This was based on the use of divergence-free stress representation which leads to self-stabilized elements without introducing internal degrees of freedom [45].

The effectiveness and robustness of the proposed approach were proved through several benchmark tests, such as thin

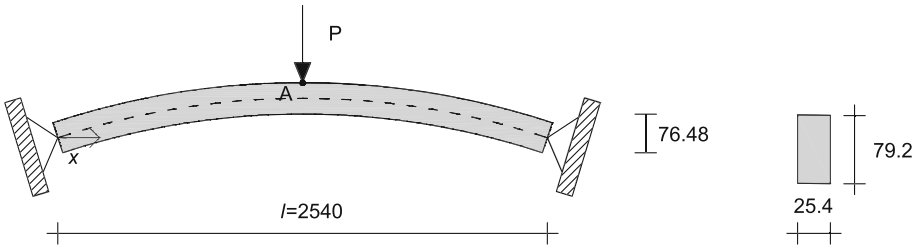

Fig. 10 Shallow arch: geometry (dimensions are in millimeters), boundary and loading conditions

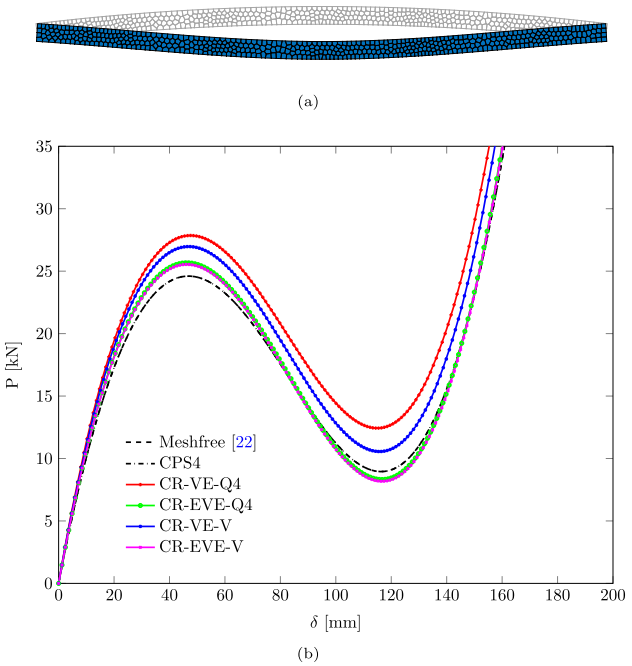

Fig. 11 Shallow arch: **a** deformed shape at the end of the analysis and **b** load–displacement curves obtained with standard and enhanced CR-VEM compared with the reference solutions obtained with the CR meshfree [22] and the Abaqus overkill mesh made of CPS4 FEs

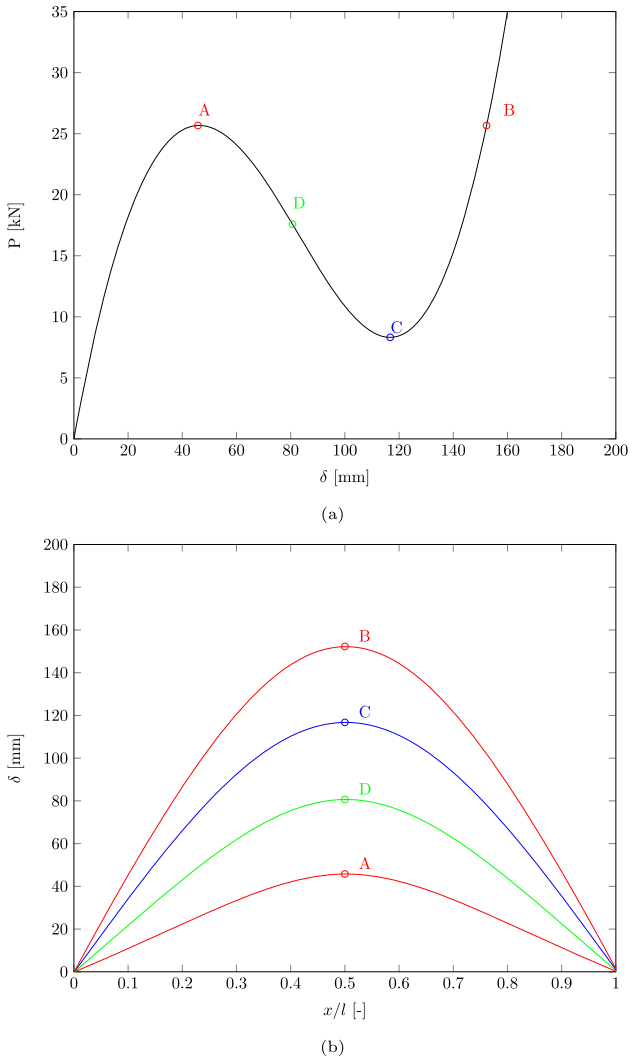

Fig. 12 Shallow arch: **a** load–displacement curve, and **b** vertical displacement along the adimensional x/l, where l is the span length. These results refer to a mesh made of CR-EVE-Q4 elements with 1390 DOFs

and thick cantilevers, an L-bracket beam, and a circular shallow arch, by adopting both quadrilateral 4-node elements and Voronoi elements with varying numbers of nodes.

An overall agreement emerged between the results obtained with the proposed CR-EVE formulation and those derived from finite element reference analyses as well as available analytical solutions. Very accurate solutions were achieved with the strain-enhanced virtual elements, also adopting coarse domain discretizations as compared to the other numerical reference solutions. Nevertheless, the limit of the corotational approach, attributable to the description of the nonlinear geometric effects only due to the nodal large displacements and rotations, emerged especially in the analysis of the response of the thick cantilever.

To conclude, the performed analyses confirm the reliability of the CR approach within the VEM framework and point out the capability of the enhanced strain representation to generate self-stabilized elements also in the nonlinear geometric range.

Further studies, herein limited to the assumption of linear elastic constitutive behavior, will be moved to a nonlinear constitutive regime to develop a tool for fully nonlinear analyses. Finally, the effectiveness of the formulation will be checked against some real structural problems.

Acknowledgements D.A. and C.G. acknowledge the grant PNRR PE5-CHANGES-Spoke 7 (CUP: B53C22003780006). E.B. and M.N. gratefully acknowledge the financial support of the Regional Agency of Civil Protection for the Emilia-Romagna Region (D.G.R. n. 686 del 14/05/2018).

Funding Open access funding provided by Università degli Studi di Ferrara within the CRUI-CARE Agreement.

Appendix A

In the following, the adopted matrix $\check{\mathbf{N}}$ with divergence-free polynomial representation is reported for the cases of:

- $q = 1$:

$$\check{\mathbf{N}} = \begin{bmatrix} 1 & 0 & 0 & y & 0 & x & 0 \\ 0 & 1 & 0 & 0 & x & 0 & y \\ 0 & 0 & 1 & 0 & 0 & -y & -x \end{bmatrix} \tag{A1}$$

- $q = 2$:

$$\check{\mathbf{N}} = \begin{bmatrix} 1 & 0 & 0 & y & 0 & x & 0 & 2xy & 0 & x^2 & y^2 & 0 \\ 0 & 1 & 0 & 0 & x & 0 & y & 0 & 2xy & y^2 & 0 & x^2 \\ 0 & 0 & 1 & 0 & 0 & -y & -x & -y^2 & -x^2 & -2xy & 0 & 0 \end{bmatrix} \tag{A2}$$

- $q = 3$:

$$\check{\mathbf{N}} = \begin{bmatrix} 1 & 0 & 0 & y & 0 & x & 0 & x^2 & y^2 & 0 & 0 & -2xy & x^3 & y^3 & 0 & 3x^2y & 0 & -3y^2x \\ 0 & 1 & 0 & 0 & x & 0 & y & y^2 & 0 & x^2 & -2xy & 0 & 3y^2x & 0 & x^3 & y^3 & -3x^2y & 0 \\ 0 & 0 & 1 & 0 & 0 & -y & -x & -2xy & 0 & 0 & x^2 & y^2 & -3x^2y & 0 & 0 & -3y^2x & x^3 & y^3 \end{bmatrix} \tag{A3}$$

References

1. Wempner G (1969) Finite elements, finite rotations and small strains of flexible shells. Int J Solids Struct 5(2):117–153. https://doi.org/10.1016/0020-7683(69)90025-0
2. Belytschko T, Hsieh BJ (1973) Non-linear transient finite element analysis with convected co-ordinates. Int J Numer Meth Eng 7(3):255–271. https://doi.org/10.1002/nme.1620070304
3. Argyris JH, Balmer H, Doltsinis JS, Dunne PC, Haase M, Kleiber M, Malejannakis GA, Mlejnek H-P, Müller M, Scharpf DW (1979) Finite element method—the natural approach. Comput Methods Appl Mech Eng 17–18:1–106. https://doi.org/10.1016/0045-7825(79)90083-5
4. Mattiasson K, Bengtsson A, Samuelsson A (1985) On the accuracy and efficiency of numerical algorithms for geometrically nonlinear structural analysis
5. Belytschko T, Bindeman LP (1993) Assumed strain stabilization of the eight node hexahedral element. Comput Methods Appl Mech Eng 105(2):225–260
6. Liu WK, Guo Y, Tang S, Belytschko T (1998) A multiple-quadrature eight-node hexahedral finite element for large deformation elastoplastic analysis. Comput Methods Appl Mech Eng 154(1–2):69–132
7. Masud A, Tham CL, Liu WK (2000) A stabilized 3-D co-rotational formulation for geometrically nonlinear analysis of multi-layered composite shells. Comput Mech 26(1):1–12
8. Crisfield MA (1990) A consistent co-rotational formulation for non-linear, three-dimensional, beam-elements. Comput Methods Appl Mech Eng 81(2):131–150. https://doi.org/10.1016/0045-7825(90)90106-V
9. Di Re P, Addessi D (2018) A mixed 3D corotational beam with cross-section warping for the analysis of damaging structures under large displacements. Meccanica 53(6):1313–1332
10. Crisfield MA, Moita GF (1996) A co-rotational formulation for 2-D continua incompatible modes. Int J Numer Meth Eng 39(15):2619–2633. https://doi.org/10.1002/(SICI)1097-0207(19960815)39:15<2619::AID-NME969>3.0.CO;2-N
11. Battini J-M (2008) A non-linear corotational 4-node plane element. Mech Res Commun 35(6):408–413. https://doi.org/10.1016/j.mechrescom.2008.03.002
12. Battini J-M (2007) A modified corotational framework for triangular shell elements. Comput Methods Appl Mech Eng 196(13–16):1905–1914. https://doi.org/10.1016/j.cma.2006.10.006
13. Crisfield MA, Moita GF (1996) A unified co-rotational framework for solids, shells and beams. Int J Solids Struct 33(20):2969–2992. https://doi.org/10.1016/0020-7683(95)00252-9
14. Macorini L, Izzuddin BA (2011) A non-linear interface element for 3D mesoscale analysis of brick-masonry structures. Int J Numer Meth Eng 85(12):1584–1608. https://doi.org/10.1002/nme.3046

15. Felippa CA, Haugen B (2005) A unified formulation of small-strain corotational finite elements: I. Theory. Comput Methods Appl Mech Eng 194(21–24):2285–2335. https://doi.org/10.1016/j.cma.2004.07.035
16. Addessi D, Di Re P, Sacco E (2020) Corotational Beam-interface model for stability analysis of reinforced masonry walls. In: Carcaterra A, Paolone A, Graziani G (eds) Proceedings of XXIV AIMETA conference 2019. Springer, Cham, pp 1939–1953
17. Addessi D, Di Re P, Sacco E (2020) Micromechanical and multiscale computational modeling for stability analysis of masonry elements. Eng Struct 211:110428
18. Bisegna P, Caselli F, Marfia S, Sacco E (2014) A new SMA shell element based on the corotational formulation. Comput Mech 54(5):1315–1329. https://doi.org/10.1007/s00466-014-1061-x
19. Khosravi P, Ganesan R, Sedaghati R (2008) An efficient facet shell element for corotational nonlinear analysis of thin and moderately thick laminated composite structures. Comput Struct 86(9):850–858
20. Caselli F, Bisegna P (2014) A corotational flat triangular element for large strain analysis of thin shells with application to soft biological tissues. Comput Mech 54(3):847–864. https://doi.org/10.1007/s00466-014-1038-9
21. Garcea G, Madeo A, Casciaro R (2012) The implicit corotational method and its use in the derivation of nonlinear structural models for beams and plates. J Mech Mater Struct 7(6):509–538
22. Yaw LL, Sukumar N, Kunnath SK (2009) Meshfree co-rotational formulation for two-dimensional continua. Int J Numer Meth Eng 79(8):979–1003. https://doi.org/10.1002/nme.2606
23. Arroyo M, Ortiz M (2006) Local maximum-entropy approximation schemes: a seamless bridge between finite elements and meshfree methods. Int J Numer Meth Eng 65(13):2167–2202
24. De Veiga LB (2010) A mimetic finite difference method for linear elasticity. M2AN Math Model Numer Anal 44(2):231–250
25. Sukumar N, Tabarraei A (2004) Conforming polygonal finite elements. Int J Numer Meth Eng 61(12):2045–2066
26. Tabarraei A, Sukumar N (2006) Application of polygonal finite elements in linear elasticity. Int J Comput Methods 3(04):503–520
27. Chi H, Talischi C, Lopez-Pamies O, H. Paulino G (2015) Polygonal finite elements for finite elasticity. Int J Numer Methods Eng 101(4):305–328
28. Veiga L, Brezzi F, Cangiani A, Manzini G, Marini LD, Russo A (2013) Basic principles of virtual element methods. Math Models Methods Appl Sci 23(01):199–214
29. Artioli E, Veiga L, Lovadina C, Sacco E (2017) Arbitrary order 2D virtual elements for polygonal meshes: part I, elastic problem. Comput Mech 60(3):355–377. https://doi.org/10.1007/s00466-017-1404-5
30. Taylor R, Artioli E (2018) Vem for inelastic solids. In: Onate E, Peric D, de Souza Neto E, Chiumenti M (eds) Advances in computational plasticity: a book in Honour of D. Roger J. Owen. Springer, Berlin, pp 381–394
31. Artioli E, Veiga L, Lovadina C, Sacco E (2017) Arbitrary order 2D virtual elements for polygonal meshes: part II, inelastic problem. Comput Mech 60(4):643–657. https://doi.org/10.1007/s00466-017-1429-9
32. Aldakheel F, Hudobivnik B, Wriggers P (2019) Virtual element formulation for phase-field modeling of ductile fracture. Int J Multiscale Comput Eng 17(2):181–200
33. Artioli E, Marfia S, Sacco E (2020) VEM-based tracking algorithm for cohesive/frictional 2D fracture. Comput Methods Appl Mech Eng 365:112956. https://doi.org/10.1016/j.cma.2020.112956
34. Benvenuti E, Chiozzi A, Manzini G, Sukumar N (2022) Extended virtual element method for two-dimensional linear elastic fracture. Comput Methods Appl Mech Eng 390:114352
35. Chi H, Veiga LB, Paulino GH (2017) Some basic formulations of the virtual element method (VEM) for finite deformations. Comput Methods Appl Mech Eng 318:148–192. https://doi.org/10.1016/j.cma.2016.12.020
36. Wriggers P, Reddy B, Rust W, Hudobivnik B (2017) Efficient virtual element formulations for compressible and incompressible finite deformations. Comput Mech 60:253–268
37. Berrone S, Borio A, Marcon F (2021) Lowest order stabilization free virtual element method for the Poisson equation. arXiv preprint arXiv:2103.16896
38. Nagtegaal JC, Parks DM, Rice J (1974) On numerically accurate finite element solutions in the fully plastic range. Comput Methods Appl Mech Eng 4(2):153–177
39. William KJ (1969) Finite element analysis of cellular structures. University of California, Berkeley
40. Hughes TJ (1980) Generalization of selective integration procedures to anisotropic and nonlinear media. Int J Numer Meth Eng 15(9):1413–1418
41. Simo J, Hughes T (1986) On the variational foundations of assumed strain methods. J Appl Mech 53(1):51–54. https://doi.org/10.1115/1.3171737
42. Simo JC, Rifai M (1990) A class of mixed assumed strain methods and the method of incompatible modes. Int J Numer Meth Eng 29(8):1595–1638
43. Belytschko T, Bachrach W (1986) Efficient implementation of quadrilaterals with high coarse-mesh accuracy. Comput Methods Appl Mech Eng 54(3):279–301
44. Simo J-C, Armero F (1992) Geometrically non-linear enhanced strain mixed methods and the method of incompatible modes. Int J Numer Meth Eng 33(7):1413–1449
45. D'Altri AM, Miranda SD, Patruno L, Sacco E (2021) An enhanced VEM formulation for plane elasticity. Comput Methods Appl Mech Eng 376:113663. https://doi.org/10.1016/j.cma.2020.113663
46. Chen A, Sukumar N (2023) Stabilization-free serendipity virtual element method for plane elasticity. Comput Methods Appl Mech Eng 404:115784
47. Lamperti A, Cremonesi M, Perego U, Russo A, Lovadina C (2023) A Hu–Washizu variational approach to self-stabilized virtual elements: 2D linear elastostatics. Comput Mech 71:1–21
48. Talischi C, Paulino GH, Pereira A, Menezes IFM (2012) PolyMesher: a general-purpose mesh generator for polygonal elements written in Matlab. Struct Multidiscip Optim 45(3):309–328. https://doi.org/10.1007/s00158-011-0706-z
49. Karkon M, Rezaiee-Pajand M (2016) Geometrical nonlinear analysis of plane problems by corotational formulation. J Eng Mech 142(10):04016073. https://doi.org/10.1061/(ASCE)EM.1943-7889.0001133
50. Liu K, Paulino GH (2017) Nonlinear mechanics of non-rigid origami: an efficient computational approach. Proc R Soc A Math Phys Eng Sci 473(2206):20170348. https://doi.org/10.1098/rspa.2017.0348
51. Yaw LL (2008) Co-rotational meshfree formulation for large deformation inelastic analysis of two-dimensional structural systems. University of California, Davis
52. Abaqus (2011) Abaqus 6.11. Dassault Systemes Simulia Corporation, Providence, RI, USA
53. Pretti G, Coombs WM, Augarde CE (2022) A displacement-controlled arc-length solution scheme. Comput Struct 258:106674